











An Optical Distortion Solution for the Keck I OSIRIS Imager

Matthew S. R. Freeman¹ , Jessica R. Lu¹ , Jim Lyke², Abhimat Gautam³ , Renate Kupke⁴ , Andrea Ghez³ ,
Shoko Sakai³ , Jay Anderson⁵ , and Andrea Bellini⁵ 

¹ UC Berkeley, USA; matthew.s.r.freeman@berkeley.edu

² W.M. Keck Observatory, USA

³ UCLA, USA

⁴ UCO Lick, USA

⁵ STSci, USA

Received 2023 April 7; revised 2023 July 24; accepted 2023 July 25; published 2023 August 23

Abstract

The astrometric precision and accuracy of an imaging camera is often limited by geometric optical distortions. These must be calibrated and removed to measure precise proper motions, orbits, and gravitationally lensed positions of interesting astronomical objects. Here, we derive a distortion solution for the OSIRIS Imager fed by the Keck I adaptive optics system at the W. M. Keck Observatory. The distortion solution was derived from images of the dense globular clusters M15 and M92 taken with OSIRIS in 2020 and 2021. The set of 403 starlists, each containing ~ 1000 stars, were compared to reference Hubble catalogs to measure the distortion-induced positional differences. OSIRIS was opened and optically realigned in 2020 November and the distortion solutions before and after the opening show slight differences at the ~ 20 mas level. We find that the OSIRIS distortion closely matches the designed optical model: large, reaching 20 pixels at the corners, but mostly low order, with the majority of the distortion in the 2nd-order mode. After applying the new distortion correction, we find a median residual of $[x, y] = [0.052, 0.056]$ pixels ($[0.51, 0.56]$ mas) for the 2020 solution, and $[x, y] = [0.081, 0.071]$ pixels ($[0.80, 0.71]$ mas) for the 2021 solution. Comparison between NIRC2 images and OSIRIS images of the Galactic center show that the mean astrometric difference between the two instruments reduces from 10.7 standard deviations to 1.7 standard deviations when the OSIRIS distortion solution is applied. The distortion model is included in the Keck AO Imaging data-reduction pipeline and is available for use on OSIRIS data.

Unified Astronomy Thesaurus concepts: [Astronomical instrumentation \(799\)](#); [Optical aberration \(2330\)](#); [Optical position \(1172\)](#)

1. Introduction

Precise, accurate, and long-term stable astrometry has been essential for a number of major observing projects at the W. M. Keck Observatory. For instance, the discovery of the Milky Way's central supermassive black hole was achieved by using astrometric measurements of stars in the Galactic center to map their orbits (Ghez et al. 2008). Astrometric measurements can also be used to measure the masses of gravitational microlenses, giving one of the few ways to discover isolated black holes (Lu et al. 2016; Lam et al. 2022). A limiting factor for these high-astrometric-precision experiments is geometric optical distortion, a shift in the positions of stars on a detector caused by aberrations in the optical path through the telescope and instrument. This shift adds uncertainty to star positions, reducing the accuracy of astrometric measurements.

Fortunately, geometric optical distortion is a function of detector position and is static with time (specifically for Nasmyth mounted systems, which do not experience gravity-induced flexure). It is therefore possible to characterize the distortion at one time and calculate a correction that can be applied to observations taken weeks, months, or even years later.

There are multiple methods to calibrate an instrument's distortion solution. Anderson & King (2002) calculated a

distortion solution for WFPC2 on the Hubble Space Telescope (HST) using a self-calibration method, where stars are repeatedly imaged at many points and different angles on the detector. This method is time consuming but reliable, and the distortion-corrected Hubble images are commonly used as a reference to calculate distortion models for other instruments. Plewa et al. (2018) calculated a distortion model for the NCAO imager at the Very Large Telescope using Hubble as an undistorted reference. Yelda et al. (2010) and Service et al. (2016) calculated the distortion for NIRC2 on Keck II, again by comparing observations to Hubble. Service et al. (2016) went a step further by iteratively refining the reference frame from the observations, to remove the reliance on Hubble.

In this paper, we derive a distortion solution for the OSIRIS Imager, an infrared instrument mounted on the left Nasmyth platform of the Keck I telescope at the W. M. Keck Observatory (Larkin et al. 2006). OSIRIS includes a spectrometer and an imager, with a field of view of $20'' \times 20''$ and a plate scale of 10 mas per pixel. The distortion requirement for OSIRIS's design was to have a comparable distortion error to NIRC2. Service et al. (2016) found NIRC2's residual distortion to be $[x, y] = [1.2, 1.0]$ mas, and we aim to generate a distortion solution with a similar level of error.

To calculate the optical distortion present in OSIRIS images, we observe stars with OSIRIS and compare their observed positions to a reference catalog with the true star positions. Any differences are due to optical distortion in OSIRIS. This is similar to the method used in Yelda et al. (2010) and Service et al. (2016) for NIRC2. This method requires stars to be

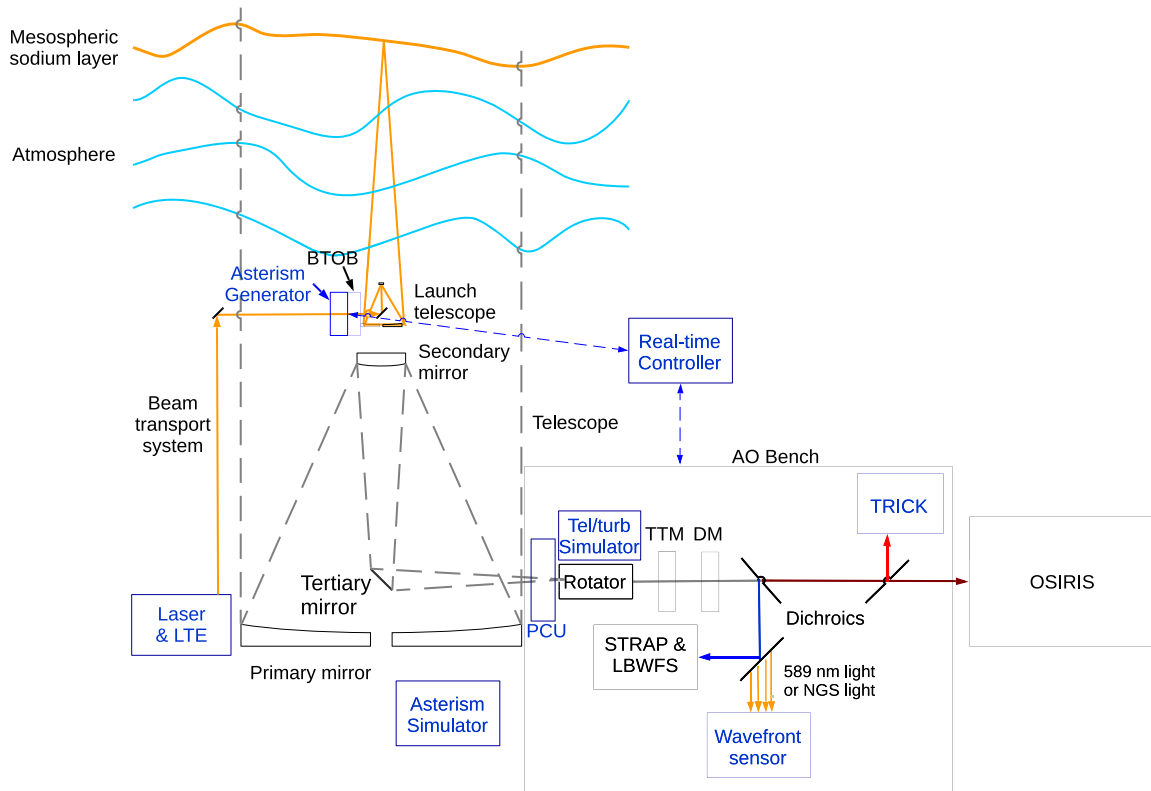


Figure 1. A diagram of the Keck I telescope, showing the optical path through to OSIRIS. The precision calibration unit (PCU) is mounted at the front of the bench. The deformable mirror and the dichroics that split light off to the wavefront sensor and TRICK could potentially be sources of distortion (modified from Figure 1 of Wizinowich et al. 2020).

observed at many points on the detector, to densely sample the distortion. To achieve this, we observed the globular clusters M15 and M92, which feature dense fields of bright stars, and dithered the field of view in steps of $5''$, to have stars repeatedly sampled at different locations.

We also require an accurate reference catalog, with no optical distortion. We use Hubble catalogs of M15 from Bellini et al. (2014) and M92 from Anderson et al. (2008), which already have Hubble’s distortion correction applied, and so should have minimal distortion. However, residual distortions may remain, so in Section 3.7 we generate a new reference frame from the OSIRIS data, removing the reliance on the Hubble catalog.

The current version of the OSIRIS Imager was installed on Keck I on 2018 March 30. The previous version of OSIRIS had a smaller 1024×1024 detector, and the distortion solution we calculate does not apply to it. OSIRIS was opened on 2020 November 16 to repair the spectrometer lenslet mask, and the optics were realigned when it was closed. This could have shifted some of the optics and altered the distortion solution. Therefore, we derive a 2020 solution for before OSIRIS was opened, and a 2021 solution for after it was opened.

Keck I includes several optics that could potentially affect the distortion solution (shown in Figure 1). These include the deformable mirror, and the dichroics that split light off to the wavefront sensor and TRICK, the infrared tip-tilt sensor (Wizinowich et al. 2014). The wavefront sensor dichroic is always in place, so will be included in the static distortion model. Similarly, the deformable mirror is calibrated each observing run during adaptive optics (AO) checkout. The TRICK dichroic, however, is inserted into the beam when

TRICK is in use, which may alter the distortion, and so should be accounted for by calculating the distortion with and without the TRICK dichroic in the beam.

2. Observations

The OSIRIS Imager was used to observe the globular clusters M15 and M92 in 2020 and 2021. M15 (R.A. 21:29:58.33, decl. 12:10:01.20) was observed using the Kn3 filter ($\lambda = 2175.6$ nm, $\Delta\lambda = 108.1$ nm) on one night in 2020 and one night in 2021. M92 (R.A. = 17:17:07.39, decl. = 43:08:09.40) was observed using the Kp filter ($\lambda = 2114.5$ nm, $\Delta\lambda = 307.0$ nm) on three nights in 2020. OSIRIS is fed by Keck I’s Single-Conjugate Adaptive Optics system, which includes a sodium laser guide star (LGS). All observations were performed in LGS mode, using a visible-light tip-tilt star with STRAP (even when the H -band TRICK dichroic was in). The M15 observations were of higher quality, with Strehl ratios of ~ 0.4 – 0.5 and mean FWHMs of ~ 50 mas, compared to the M92 observations with Strehl ratios of ~ 0.1 and mean FWHMs of ~ 70 – 120 mas. The observations are summarized in Table 1 and an example reduced frame is shown in Figure 2.

The observations were dithered in a wide grid pattern with approximately $5''$ steps, shown in Figure 3, and taken with the multiple position angles (PAs) listed in Table 1. At each grid position a set of 12 frames is taken, usually containing four small dithers with three frames at each position. The wide dither pattern ensures that stars are sampled at many points on the detector, and that the same stars are sampled in different locations. The multiple PAs separate out systematic effects—the optical distortion will appear fixed with the detector frame,

Table 1
OSIRIS Observations of Globular Clusters

UT Date	Target	Raw Frames	Integration Time (s)	Co-adds	Filter	Trick Dichroic	PAs	Mean Strehl	Mean FWHM (mas)
2020-07-31	M92	10	1.475	10	Kp	Open	0°	0.133 ± 0.029	69.0 ± 28.1
2020-08-04	M15	177	2.950	10	Kn3	Open	0°, 90°	0.524 ± 0.067	47.6 ± 1.4
2020-08-13	M92	10	5.901	1	Kp	Open	0°	0.095 ± 0.014	123.5 ± 23.2
2020-08-14	M92	20	2.950	10	Kp	Open	0°	0.097 ± 0.018	91.3 ± 25.6
2021-10-24	M15	186	2.950	10	Kn3	<i>H</i> band	0°, 22.5°, 42.5°, 122.5°	0.389 ± 0.103	52.4 ± 5.9

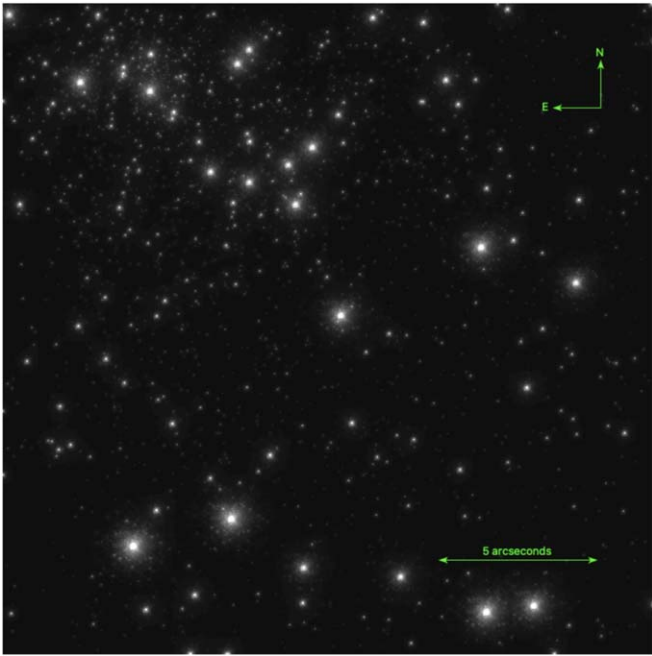


Figure 2. A reduced and cleaned OSIRIS image of M15 in the Kn3 band from UT 2021 October 24.

while systematic effects in the true star position will rotate with the PA.

Distortions must be calibrated with an identical optical path through the AO system and instrument, for both the calibration and science observations. However, the Keck I AO system optics can be configured differently when using optical (STRAP) versus infrared (TRICK) tip-tilt guiding. In TRICK mode a dichroic is inserted into the optical path to split off either H -band or K -band light to TRICK. This dichroic may introduce additional distortion (Rampy et al. 2015), so observations were taken with the dichroic in the beam (H band) and out of the beam (open). Unfortunately, we only managed to take observations with the TRICK dichroic in the open position in 2020, and in the H -band position in 2021, so we currently cannot separate any distortion due to the dichroic from the effect of opening and realigning OSIRIS.

2.1. Test Galactic Center Observations

In Section 4.1, we test the distortion solution on some Galactic center data by comparing a separate set of observations taken with OSIRIS to observations taken with NIRC2. This data set includes 71 OSIRIS observations of the Galactic center (R.A. 17:45:40.24 h, decl. $-29:00:26.8$ deg) from UTC 2021 July 26, along with 228 NIRC2 observations of the Galactic center (R.A. 17:45:40.08 hr, decl. $-29:00:30.2$ deg) from UTC 2021 July 22. The OSIRIS images were taken in the $Kn3$ band using STRAP, with a PA of 0.01° . The NIRC2 images were taken in the Kp band with a PA of 0.7° . The NIRC2 observing configuration is the same as in Stolte et al. (2008) and Ghez et al. (2008). These observations are summarized in Table 2.

3. Methods

To calculate the OSIRIS distortion solution, we go through a number of steps. First, we reduce the OSIRIS observations (Section 3.1) and extract the star positions (Section 3.2) to

produce a starlist of observations. Normally differential atmospheric refraction (DAR) would be subtracted from the observations in the reduction step, but that requires the positions of stars to be precisely known, which we cannot do without a distortion model. Instead, we add the inverse DAR correction to the Hubble reference frame (Section 3.3). With the OSIRIS observations reduced and the Hubble reference frame corrected, we then match the stars in each list (Section 3.4) and calculate the four-parameter transformation between them. We then fit a Legendre polynomial to the remaining difference vectors between stars, which gives us our distortion solution (Section 3.8). To improve the four-parameter transformation, we go back and apply the distortion model to the observations, and iteratively repeat the matching and fitting procedures (Section 3.5), calculating an updated distortion solution each time. To remove any residual distortion in the Hubble reference frame, we generate a new reference frame by combining the OSIRIS starlists (Section 3.7), and iteratively repeat the entire procedure with the updated reference frame. The distortion solution from the last iteration becomes our final distortion model. These steps are laid out in the flowchart in Figure 4.

3.1. Data Reduction

The OSIRIS images of M15 and M92 were reduced with the Keck AO Imaging (KAI) data-reduction pipeline (Lu 2022). KAI performs dark and sky subtraction, flat-field correction, and bad pixel and cosmic-ray correction. The Strehl ratios and FWHM are calculated on the individual exposures. Mean Strehl ratios and FWHMs are reported in Table 1. The KAI pipeline would normally apply corrections for instrumental distortion and DAR, but these steps first require a distortion solution, so are skipped for now.

The Hubble catalogs for M15 and M92 list the star positions in a rectified Cartesian coordinate system, with respect to the adopted center of the cluster. The observations are from 2006, so the Hubble star positions are projected forward to the same epoch as each OSIRIS image, using the proper motions listed in the catalog.

3.1.1. Galactic Center Data Reduction

The NIRC2 and OSIRIS observations of the Galactic center from Section 2.1 were also reduced using KAI, in single point-spread function (PSF) mode. The Galactic center images were stacked to produce a single deep exposure for source extraction and three, equal-depth subset exposures used for estimating uncertainties. This step was performed after we calculated the final OSIRIS distortion solution, so distortion correction and DAR correction could be performed as normal. The NIRC2 observations were reduced using the existing NIRC2 distortion solution from Service et al. (2016). For more information on the reduction of NIRC2 Galactic center data, see Jia et al. (2019). For the OSIRIS observations, the reduction was repeated twice: once with our distortion solution applied, and once without our distortion solution, to compare them (see Section 4.1).

3.2. Source Extraction

The positions and fluxes of stars were extracted from individual images using PSF-fitting routines. We utilized the AIROPA package (Witzel et al. 2016), which runs the

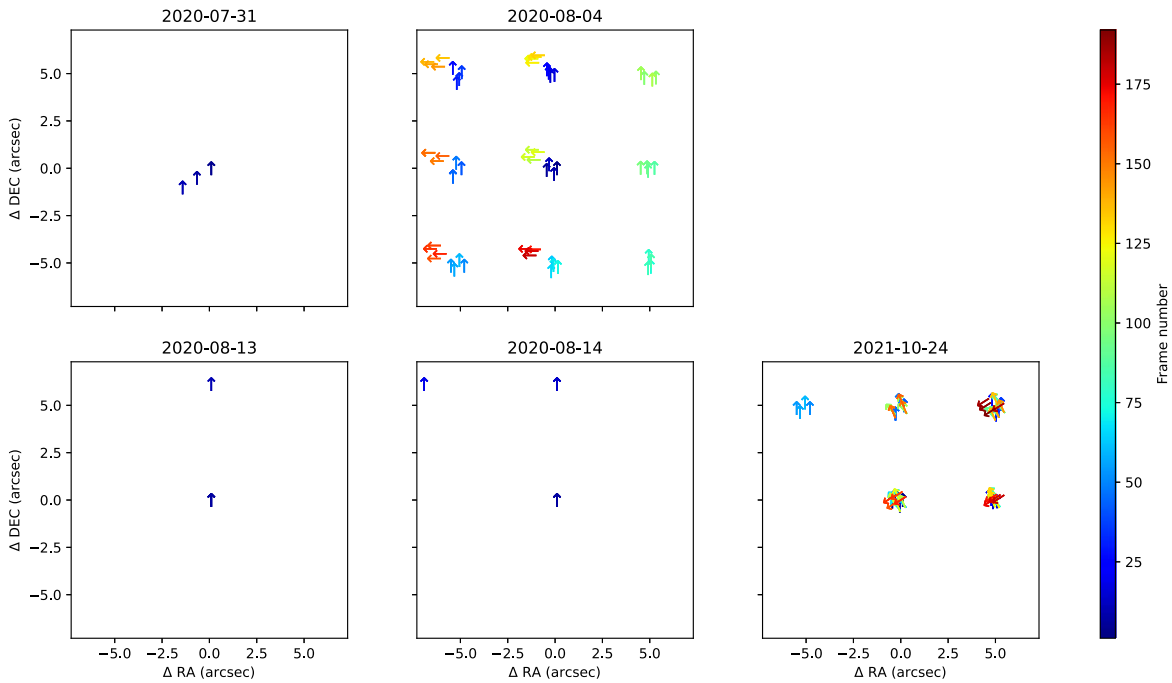


Figure 3. The dither pattern of observations in Table 1. Each marker shows the R.A. and decl. of the telescope for a frame, calculated from the header keywords TARGRA+RAOFF and TARGDEC+DECOFF, and given in arcseconds relative to the first observation of the night. The direction of the arrow shows the position angle (PA) of the observation. The color bar corresponds to the frame number of each image on that night. Typically, three frames are taken at each pointing.

Table 2
Galactic Center Observations

Instrument	UT Date	Raw Frames	Integration Time (s)	Co-adds	Filter	Mean Strehl	Mean FWHM (mas)
OSIRIS	2021-07-26	71	1.476	20	Kn3	0.359 ± 0.071	52.5 ± 3.6
NIRC2	2021-07-22	228	2.8	10	Kp	0.382 ± 0.039	59.5 ± 3.5

Starfinder algorithm (Diolaiti et al. 2000) to find stars and return a starlist. Images of the globular clusters were not yet stacked, and were instead analyzed individually.

The stellar positions and fluxes were extracted using PSF fitting. For this analysis, we assumed that the PSF was uniform over the field of view. The PSF was extracted from the images themselves using a sample of bright, relatively isolated PSF stars we selected. By using this single-PSF model, we are assuming that the distortion only affects the position of the PSF and not its shape. It is likely that distortion does in fact have some effect on the shape of the PSF, but we do not investigate it here. The distortion solution we find will be appropriate for analyses that also detect stars using a single PSF.

Each group of starlists taken at the same R.A., decl., and PA on the same night (typically three frames) was cross-matched and combined. For each combined starlist, we used the mean and standard deviation of each star’s position and flux to estimate measurement errors. The measurement errors will later be used to weight the transformation in Section 3.8, and are listed in Table 3.

3.3. Differential Atmospheric Refraction

Light passing through the atmosphere is refracted based on its angle from the zenith. This DAR compresses the apparent position of stars in the direction of the zenith, and can shift stars by several milliarcseconds over the OSIRIS field of view. An

example of the effect over the OSIRIS field of view is shown in Figure 5.

The effect of DAR can be calculated based on the telescope R.A. and decl. and the atmospheric conditions at the time of the observation. The KAI reduction pipeline has a function to automatically download atmospheric data from KECK and calculate DAR, based on the work in Yelda et al. (2010).

Normally, the KAI pipeline would first apply a distortion correction to observations and then subtract DAR from them. However, since there is uncorrected distortion in our OSIRIS frames, we do not know the true positions of the stars and DAR correction cannot be safely applied. Instead, we added DAR to the reference frame, producing what would be seen by Keck at the bottom of the atmosphere (Figure 4, flowchart box 1). This produced a different HST+DAR reference-frame starlist for each OSIRIS image observed. The OSIRIS starlists could then be matched to their corresponding reference frames.

3.4. Star Matching

The OSIRIS starlists (in pixel coordinates) were matched to the reference starlists (in milliarcseconds) using a triangle-matching algorithm (Figure 4, flowchart box 3). The algorithm is based on the method in Groth (1986). The relative magnitudes and angles of triangles of stars are unaffected by translation, rotation, and scaling between the two coordinate frames.

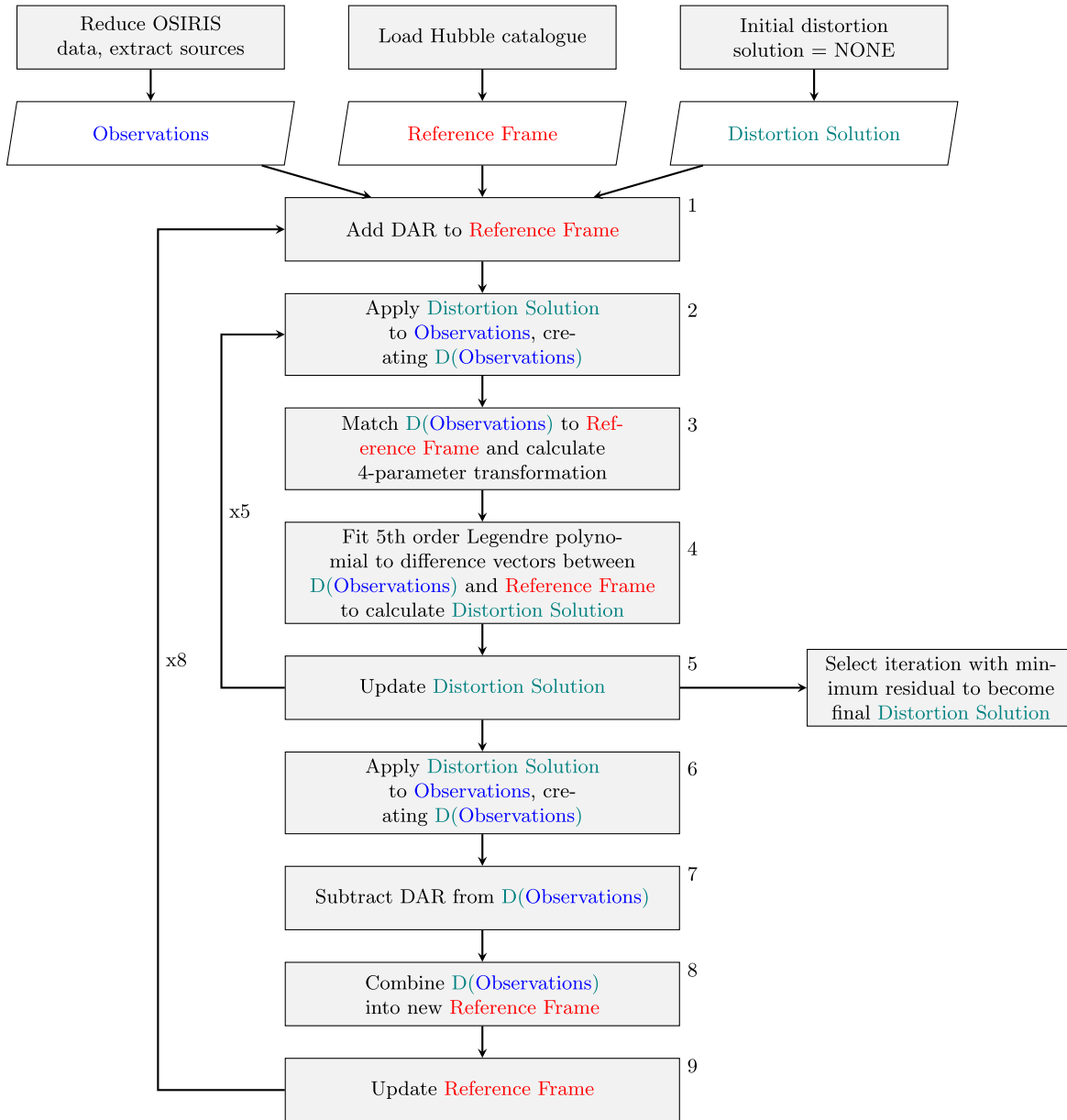


Figure 4. The steps involved in our method to calculate the distortion solution. The observations are iteratively matched to the reference frame to identify the correct four-parameter transformation (steps 2–5), and the reference frame is iteratively updated to remove any residual distortion in it (step 8).

Table 3
Sources of Error in the Distortion Solution

	Median (pixels)		Median (mas)	
	x	y	x	y
2020				
Measurement error	0.048	0.053	0.48	0.53
Distortion residual	0.0517	0.0564	0.514	0.561
Bootstrap std	0.0075	0.0044	0.075	0.044
2021				
Measurement error	0.035	0.039	0.35	0.39
Distortion residual	0.0808	0.0708	0.804	0.705
Bootstrap std	0.0056	0.0045	0.056	0.045

Note. Measurement error calculated from standard deviation of star positions across stacked frames in Section 3.2. Distortion residual from Section 4. Bootstrap error from Section 3.11.

The matching algorithm is sensitive to the number of stars, and can fail if there are too few or too many. To improve matching rates, OSIRIS stars that were 6.4 mag fainter than the brightest star in the image were discarded, as there is greater uncertainty in the positions of fainter stars. Before matching, reference catalog stars that were well outside the OSIRIS frame were temporarily discarded, to speed up the matching algorithm. OSIRIS stars detected within 5 pixels of the edge of the frame were discarded, as this region is just noise. For starlists that still failed to match, initial guesses for the transformation were manually loaded in.

3.5. Iterative Four-parameter Transformation

With the OSIRIS and reference starlists matched, we calculated a four-parameter transformation between them, to convert pixel coordinates on OSIRIS to R.A. and decl. coordinates. The four parameters of the transformation

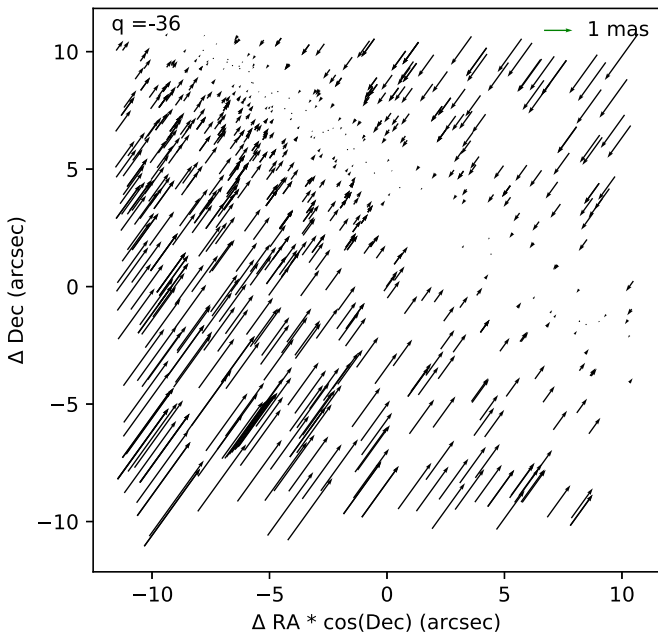


Figure 5. An example of differential atmospheric refraction (DAR) for one OSIRIS frame from 2021 October 24. DAR produces a compression in the direction of the parallactic angle q .

correspond to translation in x and y , rotation, and scale. The functional form of the transformation is described in Equation 3 of Service et al. (2019).

With the four-parameter transformation applied to the OSIRIS starlist, any remaining difference between the OSIRIS and reference starlists should be due to distortion. However, we found that the residual difference between the two starlists often showed low-order structure—translations and rotations that should have been removed by the four-parameter transformation. The four-parameter transformation derivation uses an unweighted least-squares method, entering the star coordinates into a matrix and taking the pseudoinverse, and is susceptible to numerical error. The presence of distortion between the two lists results in incorrect estimates for the four-parameter transformation parameters.

To decouple the low-order (four-parameter) residual structure from high-order distortions, we iteratively calculated the four-parameter transformation. We first calculated the four-parameter transformation between the OSIRIS starlist and the reference starlist, and used it to calculate a model for the distortion (flowchart box 4, covered in Section 3.8). We then applied that distortion model to the OSIRIS starlist (flowchart box 2) and repeated the matching, calculating the four-parameter transformation between the distortion-corrected OSIRIS starlist and the reference starlist. With the majority of the distortion removed, the remaining differences between the starlists should be more similar to a four-parameter transformation, making it easier for the algorithm to match. This iteration was repeated five times, successfully producing four-parameter transformations that did not show the residual low-order structure.

The remaining differences between the reference stars and the four-parameter-transformed observed stars are shown in Figure 6. The base of each arrow is at the location of a star on the OSIRIS detector, and the size and direction of the arrow show the difference between the star’s position in OSIRIS and

the reference list position. Here, we can start to see the shape of the OSIRIS distortion.

3.6. Outliers

To remove outliers, we divided the frame into an 8×8 grid of boxes, each containing 256×256 pixels. In each box we took the star position difference vectors from Figure 6 and calculated the Mahalanobis distance, given by $d_M = \sqrt{(\vec{x} - \vec{u})S^{-1}(\vec{x} - \vec{u})}$, where \vec{x} is the difference vector for that star, \vec{u} is the mean of the difference vectors in the box, and S is the covariance matrix of the difference vectors in the box. The Mahalanobis distance gives a multidimensional generalization of the standard deviation. Any stars that had a Mahalanobis distance greater than 3 (corresponding to 3 standard deviations away from the mean vector) were flagged as outliers and removed from the model. This procedure was repeated in a loop until no more stars were discarded. The discarded outliers in Figure 6 are colored red.

3.7. Iterative Reference Frame Generation

The Hubble reference catalog is nominally distortion corrected with a precision of 0.01–0.02 pixels = 0.5–1.0 mas (Anderson & King 2002); however, it may still contain residual uncorrected distortion, or individual stars may have different positions at optical (Hubble) versus infrared (OSIRIS) wavelengths due to binary systems or chromatic atmospheric aberrations. To correct for any residual distortions, we generate a new reference frame from the OSIRIS images. The procedure is as follows:

1. Calculate a distortion solution from the positional differences between the cross-matched and four-parameter-transformed Hubble reference catalog and the OSIRIS images (see Section 3.8, flowchart box 5).
2. Apply that distortion solution to the OSIRIS starlists (flowchart box 6).
3. Generate a new reference starlist by matching and combining all distortion-corrected OSIRIS starlists into one single list (flowchart boxes 7 and 8). The new reference list is constructed from the mean positions and fluxes of the stars with uncertainties taken as the standard deviations.
4. Repeat the distortion solution calculation in step 1, this time using the new list as the reference catalog (flowchart box 9).

This procedure is repeated over several iterations. In each iteration we reduce the residual distortion in the reference list, and so improve the distortion solution used to calculate the next iteration.

This is conceptually similar to the method that Hubble uses to calculate a distortion solution, by taking multiple images of stars at different locations on the detector and seeing how their relative positions shift (Anderson & King 2002). We are working with fewer observations here, so use the reference catalog method to get a good initial distortion model, and then use the self-matching method to improve on it.

For the 2020 solution, we ran eight of these iterations to generate a final reference frame, with the median residual decreasing from 0.222 pixels to 0.097 pixels. For the 2021 solution, we found that the median residual distortion reached a minimum after three iterations, decreasing from 0.319 pixels to 0.129 pixels, so we used this third reference frame for the final model.

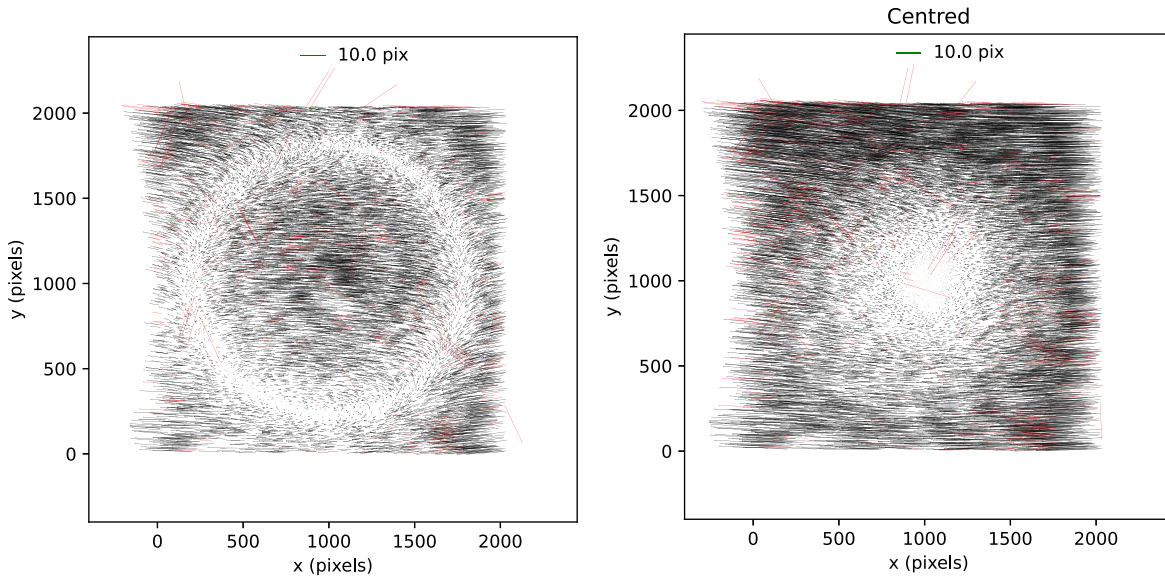


Figure 6. Map of distortion measurements for M15 observations obtained in 2021. Each vector is one measurement of a single star with the base of the arrow at the observed OSIRIS detector pixel coordinate and the arrow amplitude and direction showing the positional differences between OSIRIS positions and Hubble reference stars. Outliers are marked in red and excluded from the distortion fit. Left: distortion measurements produced by the fitting procedure, which minimizes the average distortion across the frame. Right: distortion measurements with a translation applied to set the distortion at the center of the frame to zero, revealing OSIRIS’s distortion pattern.

3.8. Legendre Polynomial Distortion Model

For this paper, we model the distortion as a two-dimensional Legendre polynomial. Legendre polynomials form a convenient orthogonal basis set, and are commonly used when modeling optical systems. The NIRC2 distortion model in Service et al. (2016) uses a Legendre polynomial. We tested a range of orders for the Legendre polynomial, from 2 to 8, covered in Section 3.10.

We fit two two-dimensional Legendre polynomials, one for the x distortion and one for the y distortion. This pair of Legendre polynomials forms the distortion solution, taking x - y pairs and outputting the corrected x' and y' coordinates. The fitting procedure is similar to Equation 6 of Service et al. (2019), using a Levenberg–Marquardt algorithm to minimize the residual.

An alternative method would be to model the distortion pixel by pixel, taking a weighted average of the nearby star for each pixel and constructing a 2048×2048 distortion map, as was done for NIRC2 by Yelda et al. (2010). However, the OSIRIS instrument was designed to have primarily low-order, smoothly varying distortions, so a polynomial model with far fewer free parameters was adopted as it is less susceptible to outliers.

3.9. Centering

The distortion solution is given relative to some arbitrary zero point, where we define there to be zero distortion. The four-parameter transformation calculation in Section 3.5 finds the transformation that produces the minimum distortion across the frame, which results in the zero point being a circular radius. For OSIRIS, it is helpful to instead set the zero point to be the center of the frame. This produces a distortion pattern that is zero in the center and increases radially.

We set the center of the frame to have zero distortion by calculating the distortion vector at the center of the frame and subtracting it from all position vectors. The difference can be seen in the left and right plots in Figure 6. Minimizing the total

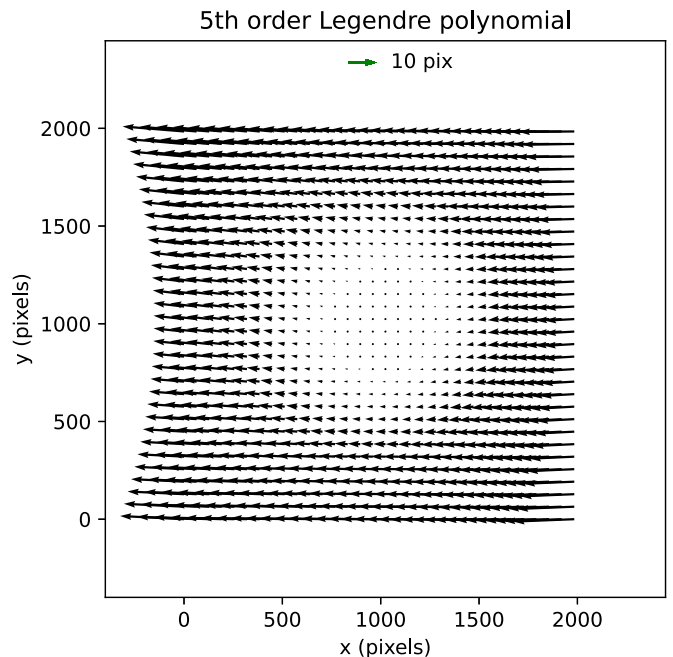


Figure 7. The 5th-order Legendre polynomial fit to the observed distortion measurements from Figure 6. This Legendre polynomial is used as the final distortion model for the 2021 data.

distortion produces the plot on the left with the apparent circular structure. Translating the solution so that the center has zero distortion produces the plot on the right, which shows how the distortion increases toward the edges.

3.10. Polynomial Order

We tested a range of orders for the Legendre polynomial fit. The model needs to have a high enough order to fit the features in the distortion, but too high an order risks overfitting. OSIRIS is designed to have low-order distortion, but higher-order

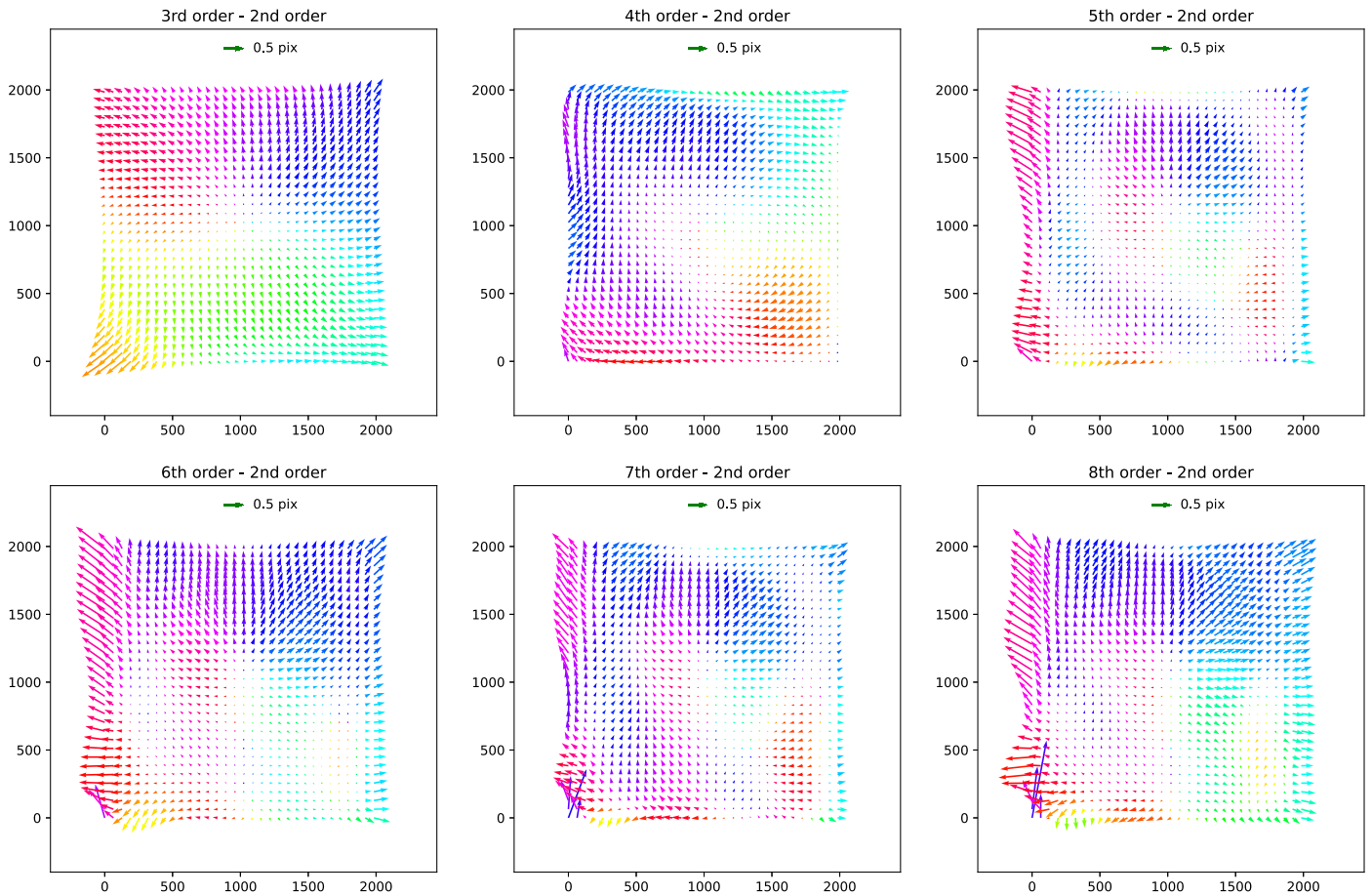


Figure 8. The difference between each higher-order polynomial model (e.g., Figure 7) and the 2nd-order model, for 2021. The colors correspond to the angle of the vector.

aberrations in the as-built instrument or from the AO system optics could still be present. To investigate this, we repeat the entire fitting procedure with polynomial orders from two to eight.

The distortion solution is dominated by low-order structure, even when fitting for higher-orders, as can be seen in the 5th-order polynomial fit shown in Figure 7. To show the effect of changing the polynomial order, we plot the differences between the 2nd-order fit and the higher-order fits in Figure 8. Structures appear on increasingly smaller scales up until the 5th-order fit; then, higher-order fits do not show structures on even smaller scales except on the edges. This suggests a 5th-order fit may be most appropriate.

We selected the optimal order for the distortion solution using an F-test on pairs of solutions, in a similar manner to Service et al. (2016). An F-test compares the goodness-of-fit of two models, scaled by the extra degrees of freedom in a higher-order model. To compare model 1 and model 2 (where model 2 has the higher order), we used

$$F = \frac{(\chi_1^2 - \chi_2^2)/(df_1 - df_2)}{\chi_2^2/df_2}, \quad (1)$$

where χ^2 is the weighted residual sum of squares, and df is the number of degrees of freedom ($df = \text{number of data points} - \text{number of parameters in model}$). A higher value for F indicates that there is a greater improvement when switching from model

1 to model 2, and a lower value for F indicates that there is less improvement.

The iterative procedure in Section 3.7 successfully matches different numbers of stars depending on how well the distortion is corrected, so to run the F-test we limited it to the stars that were matched in all polynomial order tests. The results of the F-test are shown in Figure 9.

We found much more variation in F-tests compared to Service et al. (2016). In some cases the F value was negative, indicating that the higher-order model did worse at fitting than the lower-order model. For the 2020 model, moving from a 7th-order polynomial to an 8th-order polynomial produces a very high F value, presumably because the 7th-order fit was so poor.

Disregarding the 2020 8th-order fit as an outlier, we found that moving from a 4th-order to a 5th-order polynomial produces the largest F value in both 2020 and 2021, suggesting that it is the best-fitting model. Thus, we adopted a 5th-order Legendre polynomial as our model of the distortion.

3.11. Bootstrapping Polynomial Uncertainty

To estimate the uncertainty in the Legendre polynomial fit to the data, we performed a full-sample bootstrap. In this method, we used sample-with-replacement to generate 100 new random samples of the difference vectors between the observations and the reference list (i.e., vectors in Figure 6). Each sample contained the same number of measurements as the original.

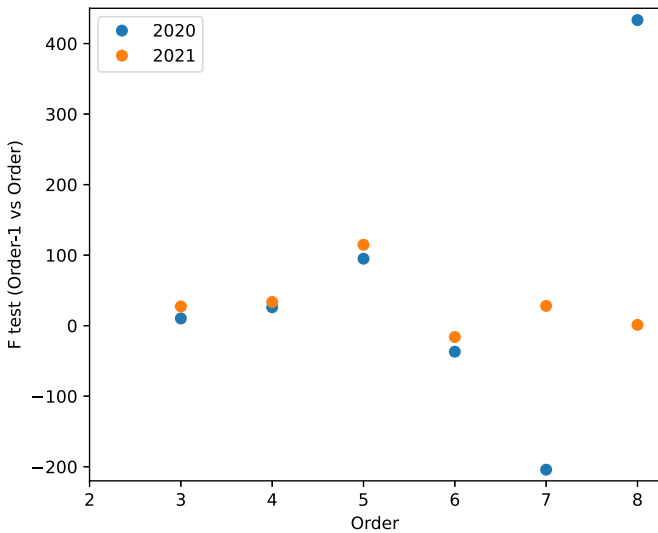


Figure 9. The results of an F-test (Equation 1) comparing each polynomial model order to the previous polynomial model order, i.e., the point labeled Order 5 is the result of an F-test comparing the 5th-order polynomial model to the 4th-order polynomial model. We find the 5th-order model to have a higher F value, indicating it is a better fit to the data.

For each sample a 5th-order Legendre polynomial fit was calculated. We then looked at each OSIRIS pixel and calculated the standard deviation in the 100 different Legendre polynomials at that point. These standard deviations are plotted in Figure 10. For 2020, we find a median standard deviation of $[x, y] = [0.0075, 0.0044]$ pixels ($[0.075, 0.044]$ mas). For 2021, we find a median standard deviation of $[x, y] = [0.0056, 0.0045]$ pixels ($[0.056, 0.045]$ mas). We see a greater uncertainty in the x direction, as there is greater distortion in the x direction. We also see greater uncertainty at the edges of the frame, where the model starts to extrapolate. These uncertainties are small compared to the residuals (Table 3), indicating that the fitting of the polynomial is not a major source of error.

4. Results

We find a 5th-order bivariate Legendre polynomial model to be the optimal balance between the quality of fit and the number of degrees of freedom, so we use this as our final distortion solution for both 2020 and 2021. The shape of the distortion can be seen in Figure 7. By defining the central pixel to have zero distortion, we see that OSIRIS’s distortion is small in the center and increases radially, with the majority of the distortion shifting stars to the negative x direction.

The 2020 solution has a mean distortion of 7.79 pixels (77.4 mas) across the field, reaching 22.95 pixels (228.2 mas) at the corners. The 2021 solution has a mean distortion of 7.60 pixels (75.7 mas) across the field, reaching 22.97 pixels (228.7 mas) at the corners.

We also evaluate the residual distortion in our model, which is the difference in position between the observed stars (with the distortion correction applied) and the reference star locations. For the 2020 fit, we find a median residual of $[x, y] = [0.052, 0.056]$ pixels or $[0.51, 0.56]$ mas. For the 2021 fit, we find a median residual of $[x, y] = [0.081, 0.071]$ pixels or $[0.80, 0.71]$ mas. The OSIRIS distortion residuals we find are slightly better than the NIRC2 distortion residuals of $[x, y] = [1.2, 1.0]$ mas from Service et al. (2016), which meets

the design requirements of OSIRIS. Figure 11 shows a quiver plot of the distortion residuals, and Figure 12 shows the weighted means of the residuals in 64×64 pixel bins.

In the 2020 distortion solution, the distortion residuals (~ 0.54 mas) are roughly consistent with the measurement error (~ 0.50 mas), with a small contribution from fitting error, as shown in Table 3. However, in 2021 the distortion residuals (~ 0.5 mas) are larger than the combined measurement error and bootstrap-fitting error. The bulk of the 2021 data had lower Strehl and image quality as compared to 2020, so it may be that PSF variations over the field, which were ignored, resulted in large systematic errors in the positions used to derive the distortion solution.

The distortion model has been added into the KAI package, and is available for use on OSIRIS Imager data. The coefficients for the Legendre polynomials are also reproduced in the Appendix, in the format used by AstroPy.

4.1. Testing the Distortion Solution on Galactic Center Data

To measure the effect of adding the distortion solution, we apply it to OSIRIS Galactic center observations, and compare the resulting astrometry to similar measurements with the already distortion-corrected NIRC2. An improved match to NIRC2 would indicate that the distortion is successfully being corrected. The NIRC2 and OSIRIS observations are described in Section 2.1, and reduced in Section 3.1.1.

The resulting OSIRIS starlists were each matched to the NIRC2 starlist with a four-parameter transformation, and the differences in star positions were recorded. We limited the analysis to stars within $4''$ of the center of the field in both the NIRC2 and OSIRIS images as there is more spatial variability in the PSF outside this radius. The stellar magnitudes were limited to $Kp < 15.5$.

Figure 13 shows histograms of the positional differences between the NIRC2 starlist and the two OSIRIS starlists: with the distortion correction applied, and with no distortion correction. Also shown are the positional differences weighted by the inverse error, which is the combination of the measurement errors in the OSIRIS and NIRC2 images and the residual distortion error. These errors are listed in Table 4.

We see a significant improvement when the distortion solution is applied, with the majority of the stars now falling within a few standard deviations from the NIRC2 positions. The mean astrometric difference between the uncorrected OSIRIS images and NIRC2 is $[x, y] = [11.7 \pm 6.0, 5.3 \pm 3.3]$ mas or $[12.2 \pm 6.8, 6.2 \pm 4.0]$ standard deviations. For the distortion-corrected OSIRIS images, the mean astrometric difference is $[x, y] = [1.5 \pm 0.9, 1.3 \pm 1.4]$ mas or $[1.5 \pm 0.9, 1.4 \pm 1.3]$ standard deviations. This is roughly consistent with the uncertainties in the distortion solutions for both NIRC2 and OSIRIS. We see a larger difference in x , as this is the direction of the majority of the OSIRIS distortion.

4.2. Plate Scale and Position Angle

With the distortion corrected, we can now precisely determine the plate scale and PA measurements for OSIRIS. We recalculated the four-parameter transformations between the distortion-corrected observations and the reference frame. These measurements are relative to Hubble’s plate scale and PA, as the reference frame is based on the Hubble catalog in

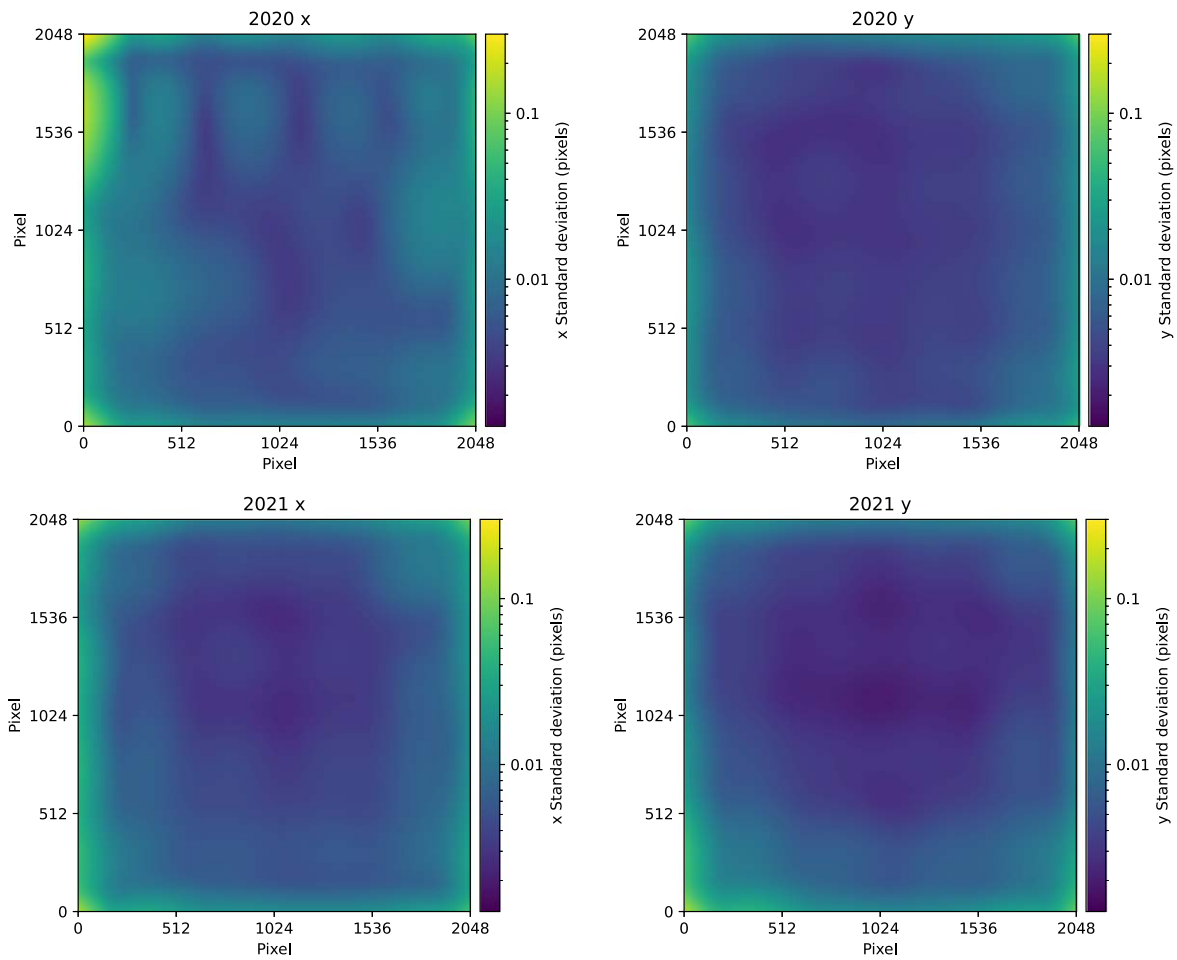


Figure 10. Legendre polynomial uncertainties calculated using bootstrapping. The color shows the standard deviation of 5th-order Legendre polynomials fit to 100 samplings of the data, for the 2020 (top) and 2021 (bottom) solutions in x (left) and y (right).

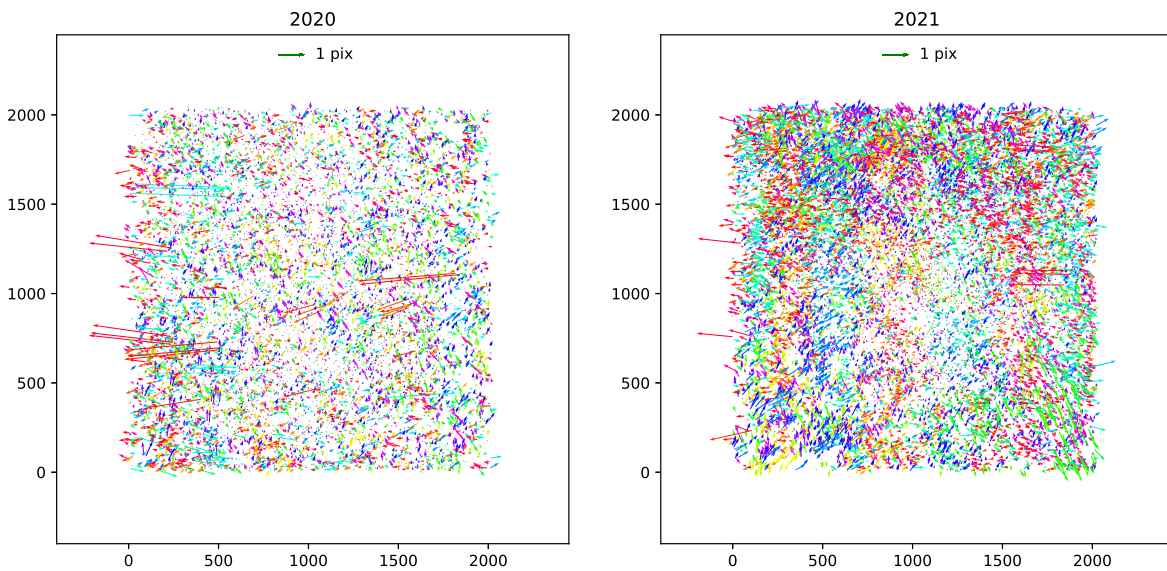


Figure 11. Residuals between the OSIRIS distortion-corrected observations of M15 and M92, and the reference-frame positions from Section 3.7. The colors correspond to the angle of the vector.

R.A. and decl. The plate scale and PA results are shown in Figure 14 as a function of UTC time on the observation night. The mean values are summarized in Table 5.

The plate scale shows variation with time. The two upper panels show the plate scale as calculated from the four-parameter transformations for each image from 2020 and 2021.

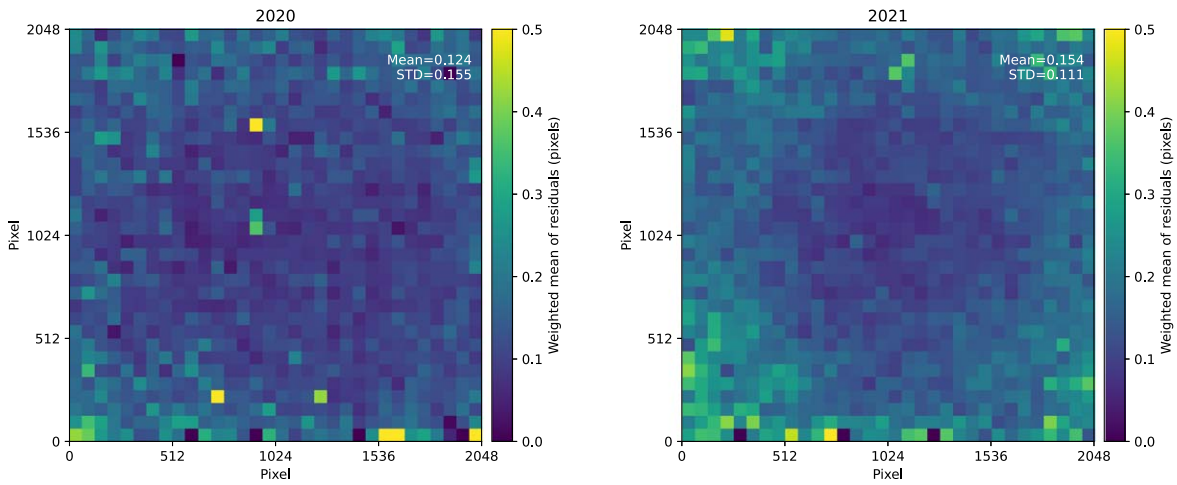


Figure 12. Weighted mean of the distortion residuals in Figure 11. Binned into 64×64 pixel bins.

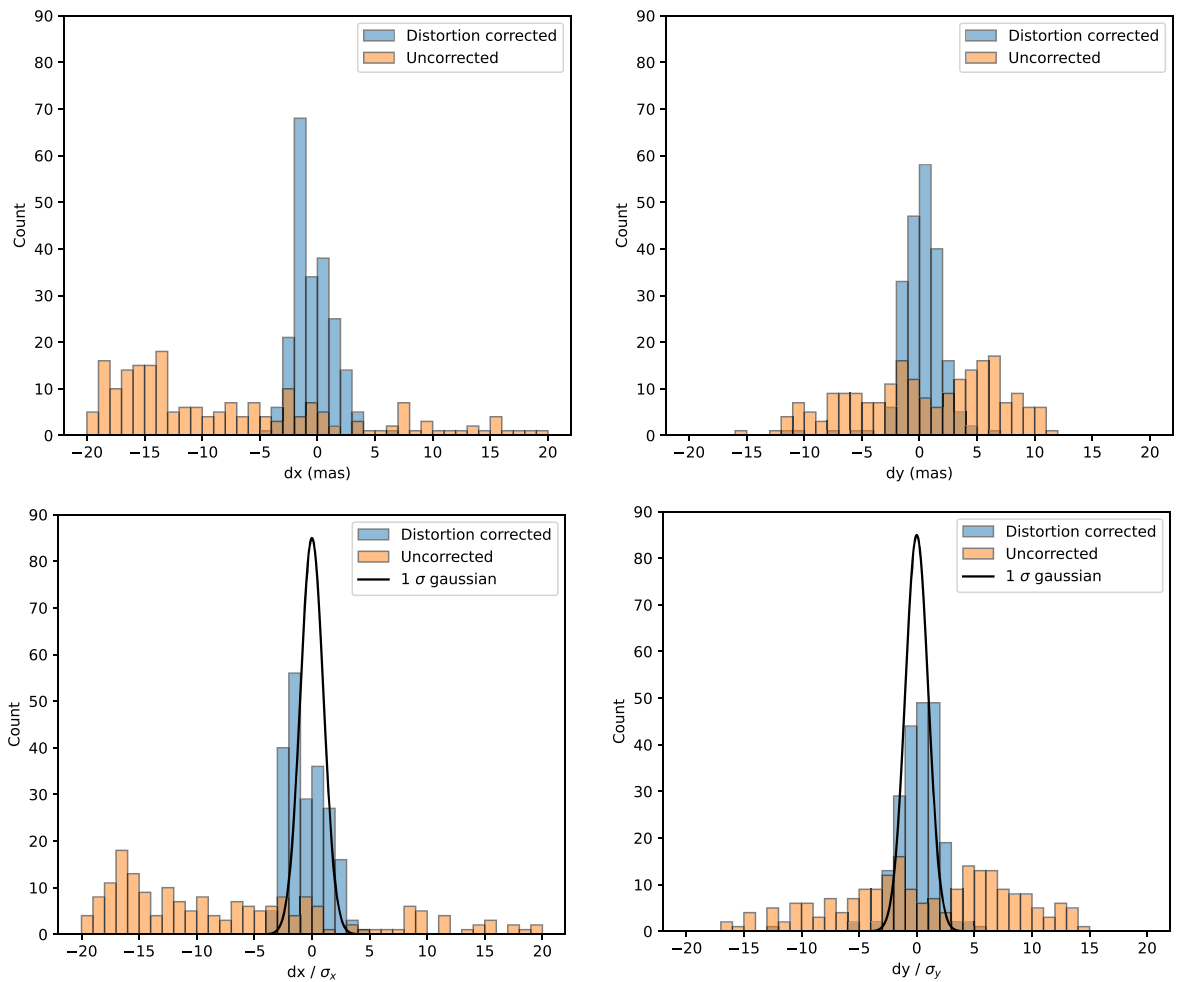


Figure 13. The difference in the x and y locations of stars between NIRC2 and OSIRIS Galactic center observations (Section 4.1), repeated with the OSIRIS distortion correction applied (blue) and without the distortion correction (orange). The top two panels show the differences dx and dy in milliarcseconds. The bottom two panels show the differences scaled by their errors σ_x and σ_y . A 1σ Gaussian is plotted for comparison.

We find the 2020 plate scale to be 9.9418 ± 0.0030 mas per pixel, and the 2021 plate scale to be 9.9576 ± 0.0010 mas per pixel. We note that the plate scale appears to be fairly constant across one night, but shows some variation between the different nights. We see a similar pattern with other telescope parameters, like the telescope temperature (TUBETEMP) and

the secondary focus (SECFOCUS), which are roughly constant across one night but show variation between nights. Movement of the focus and thermal expansion could affect the plate scale, however we do not see a correlation—greater values for the temperature or focus position do not necessarily produce greater values for the plate scale. As 2021 only contains one

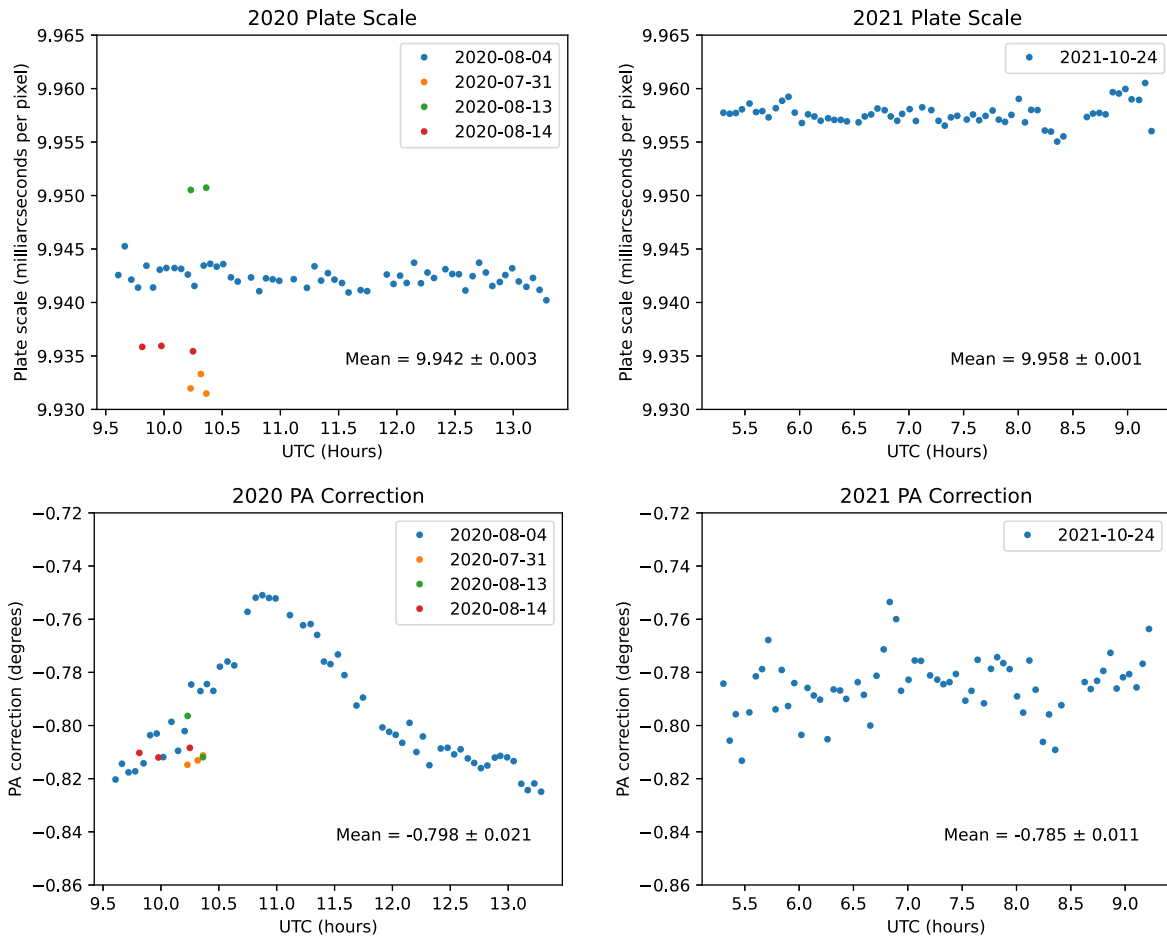


Figure 14. Calculations of the OSIRIS plate scale and the correction to the position angle, based on the four-parameter transformations to the Hubble reference frame.

Table 4
Sources of Error in the Galactic Center Test

	x (mas)	y (mas)
NIRC2 measurement error	0.331	0.318
OSIRIS with distortion measurement error	0.237	0.207
OSIRIS no distortion measurement error	0.321	0.219
Distortion residual	0.805	0.705
Distortion bootstrap	0.056	0.045

Note. Measurement errors are calculated from the standard deviation of star positions across stacked frames. Distortion residual and bootstrap errors are from Table 3.

night of data, further observations may be required to monitor its stability.

The PA set by the observer and reported in the image header shows a clear offset from the PA measured from the four-parameter transformations. The lower panels in Figure 14 show the difference between the measured PA and the PA reported in the image header keyword PA_IMAG. We find the required correction to PA_IMAG for 2020 to be $-0.798^\circ \pm 0.021^\circ$, and for 2021 we find it to be $-0.785^\circ \pm 0.011^\circ$.

The PA correction for 2020 August 4 shows a clear structure of the course of the night, with the PA increasing and decreasing over several hours. This pattern correlates with a number of the telescope’s parameters over the night: elevation,

Table 5
Mean of Plate Scale and PA Measurements

Relative to Hubble	2020	2021	
Plate scale	9.9418 ± 0.0030	9.9576 ± 0.0010	mas/pix
PA correction	-0.798 ± 0.021	-0.785 ± 0.011	degrees
Relative to NIRC2			
Plate scale		9.9566	mas/pix
PA correction		-0.659	degrees

Note. The mean plate scale shows a standard deviation of 0.0070 mas per pix across the four nights in 2020. This should be added as an additional systematic error.

parallactic angle, parallactic rate, etc. Figure 15 shows the PA correction as a function of the telescope’s elevation, showing the increase in PA correction at higher elevations. We hypothesize that this could be an error in the rotation rate of the K-mirror, causing it to lag behind the correct rotation by an amount depending on the parallactic rate. However, this pattern is not seen in 2021 October 24, which shows no correlation with elevation angle, and is inconclusive for the other three nights in 2020. More data are required to see if this pattern appears on other nights, and to determine its cause.

We also calculate the 2021 plate scale and PA relative to NIRC2, using the four-parameter transformation between the OSIRIS and NIRC2 starlists in Section 4.1. Setting NIRC2’s

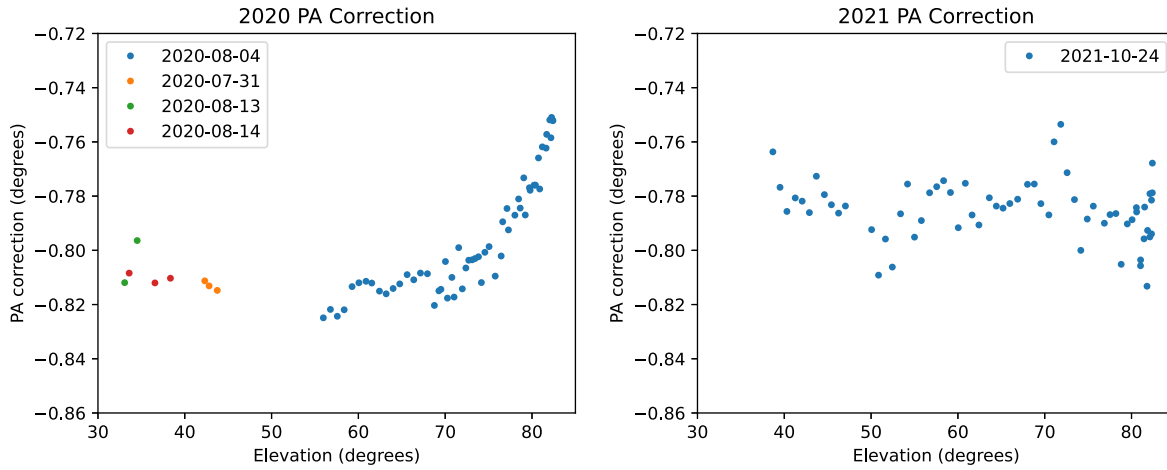


Figure 15. The measurements of the PA correction from Figure 14 as a function of telescope elevation. The data from 2020 August 4 show a correlation with elevation.

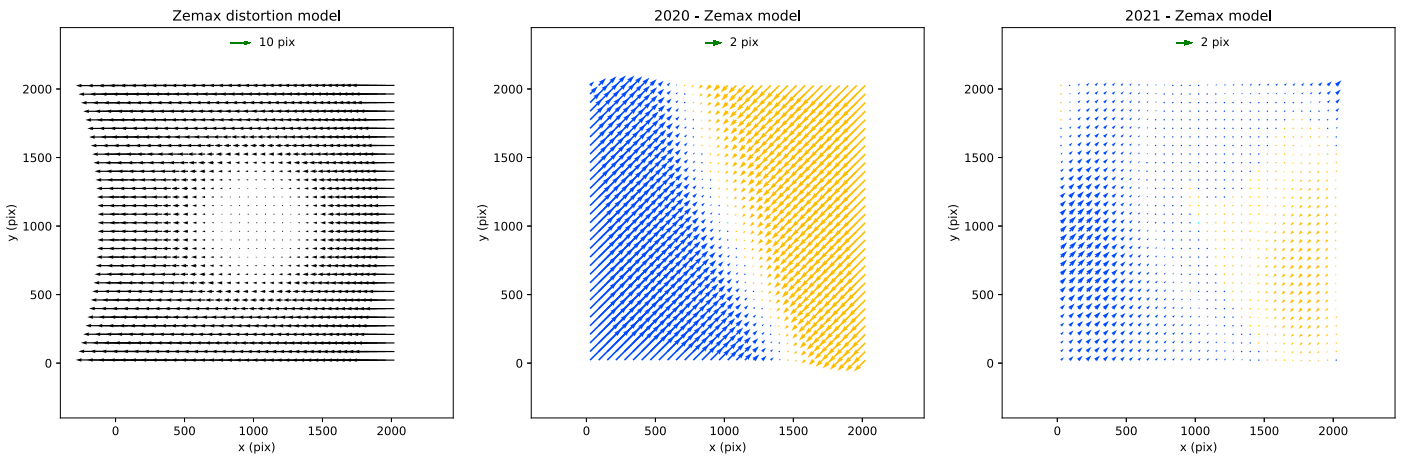


Figure 16. Left: the Zemax optical model of the OSIRIS distortion based on the nominal optical design specifications. The Zemax model was converted to pixel coordinates using the OSIRIS pixel size of $18 \mu\text{m}$. Center and right: the difference between the Zemax model and the 5th-order Legendre polynomial solutions we calculate, for 2020 and 2021 (from Figure 7). The colors correspond to the angle of the vector.

plate scale to be $9.971 \text{ mas per pixel}$ (Service et al. 2016) and using the header keyword `INSTANG = 0.7`, this calculation gives us an OSIRIS plate scale of $9.9566 \text{ mas per pixel}$, and a PA correction of -0.659° (relative to NIRC2’s PA). The plate scale we find is within the error of the measurement relative to Hubble, but the PA is not, being off by 0.12° . This result suggests that the NIRC2 PA may also need to be updated.

5. Discussion

5.1. Comparison to Zemax Model

The distortion model we find is in good agreement with the expected optical distortion based on the Zemax model of OSIRIS’s intended design. The Zemax model (which includes the dichroics for TRICK and the wavefront sensor) shows the nominal distortion but does not include any residual distortion due to manufacturing or alignment errors with the optics. The difference between the Zemax model and our Legendre polynomial model shows these residual errors.

Figure 16 shows the Zemax model of the predicted distortion (left) and the differences between this model and the 2020 and 2021 solutions. For 2020, the median difference is 2.09 pixels (20.8 mas), and for 2021 the median difference is 0.53 pixels (5.3 mas). Notably, the difference is smaller after OSIRIS was

opened at the end of 2020. This is reassuring news: opening OSIRIS and realigning the optics got it back to its intended alignment. This suggests that future work on OSIRIS can also maintain the distortion as long as the optics are properly realigned.

The Zemax model indicates the reason for the majority of the distortion being in the x direction: this distortion comes from the off-axis parabolic relay in the OSIRIS Imager, and its orientation with respect to the AO system’s off-axis parabola relay (OAP). The distortion could have been reduced by half if the beam was folded off the first OAP in the opposite direction, but there was limited space in the design.

5.2. Variable Point-spread Function

Our analysis does not use a spatially varying PSF; instead, we use a single PSF across the frame, and the solution is intended for reductions that also use a single PSF. Any field-dependent optical aberrations that shift the centroid of the PSF will be accounted for in the single-PSF distortion solution. For analyses that do include a spatially varying PSF, it may be necessary to calculate a new distortion solution that detects stars with a varying PSF. Tests with the AIROPA software package suggest that a spatially varying PSF does not significantly affect astrometric precision (Terry et al. 2022), but effects on accuracy are unknown.

5.3. Hubble versus Gaia Reference Catalogs

This work was originally carried out using a Gaia Early Data Release 3 as a reference catalog instead of the HST globular cluster data. However, with Gaia we found a low number of stars in the observed fields, and unacceptably large residuals in the resulting distortion model, with a median of 2 pixels. For our sample of Gaia stars in M15 and M92, we found that around 50% of the stars had an `astrometric_excess_noise` parameter of >2 mas. The `astrometric_excess_noise` parameter is an estimate of the uncertainty in the star's position that is not modeled by the errors (van Leeuwen et al. 2018).

The Gaia astrometry toward the M15 and M92 globular clusters is generally of poorer quality due to stellar crowding, which makes Gaia unsuitable for calibrating distortion solutions on high-resolution, small-field-of-view imagers.

6. Future Work

6.1. TRICK Dichroic

The Keck I optical path includes two dichroics that can be inserted into the beam to direct light to the TRICK infrared tip-tilt sensor. The *H*-band dichroic directs *H*-band light to TRICK, allowing *K*-band observations, and the *K*-band dichroic directs *K*-band light to TRICK, allowing observations in the *H* band and shorter.

These dichroics may introduce some distortion, so there should be separate distortion solutions for the *K* band in, the *H* band in, and neither in (open). In this paper, we only managed to get observations in the open position in 2020 and with the *H* band in in 2021, which are affected by the confounding factor of OSIRIS being opened at the end of 2020. Future distortion work should investigate whether the TRICK dichroic contributes to distortions.

6.2. Precision Calibration Unit

Calculating the distortion using on-sky observations as we have here is time consuming, requiring many observations with a range of dithers, PAs, and dichroic settings. It also requires significant computational time to generate the new reference frames, as detailed in Section 3.7.

To aid future distortion solution calculations, we have installed a precision calibration unit (PCU) on the Keck I optical bench. The PCU consists of a set of three linear stages and one rotational stage. Mounted to the rotational stage is a pinhole mask, with a grid of 24 μm pinholes at a spacing of 0.5 mm, covering a diameter of 41 mm. The linear and rotational stages allow the pinhole mask to translate in three dimensions, as well as to rotate. The PCU also mounts a fiber bundle for calibrations, and mirrors to direct light to the Keck Planet Finder and from the Telescope Simulator. It is mounted to the front of the optical bench, where it can drive the pinhole mask to a focal point in the optical path just inside the K-mirror. By back-illuminating the pinhole mask when it is at the focal point, we get a grid of artificial stars which OSIRIS can image. By comparing the apparent positions of the stars to the expected regular grid pattern, we can get an accurate measurement of the distortion.

With the PCU it should be possible to regularly measure the distortion, to monitor any variations over time or with observing setup. Using the PCU has many advantages over

the on-sky method used in this paper. The imaging can be done during the daytime, saving valuable nighttime hours. The PCU can move to new positions and rotation angles quickly, further decreasing the time required. The pinhole covers the full OSIRIS detector, giving an excellent density of measurements. Finally, the pinhole positions are well known, providing an accurate reference frame with no distortion, so the iterative reference-frame generation in Section 3.7 should not be needed.

7. Conclusions

We successfully derive a geometric optical distortion solution for the OSIRIS Imager, for 2020 and 2021. By comparing images of the globular clusters M15 and M92 to a distortion-corrected Hubble catalog, we obtain $\sim 20,000$ measurements of the distortion map across the detector. We account for any residual distortion in the Hubble catalog by iteratively generating a new reference frame using the OSIRIS images. We fit the distortion with a two-dimensional 5th-order Legendre polynomial, for both the *x* and *y* directions.

The resulting distortion models have a median residual of 0.96 mas for 2020 and 1.29 mas for 2021. Running a full-sample bootstrap gives a median uncertainty in the Legendre fit of 0.06 in *y* for 2020, and 0.05 mas for 2021. The residual errors in the distortion are $[x, y] = [0.80, 0.71]$ mas, slightly better than the required distortion residual of $[x, y] = [1.2, 1.0]$ mas.

When distortion-corrected OSIRIS observations of the Galactic center are compared to NIRC2 observations, we find the mean astrometric difference to be 1.8 standard deviations in *x* and 1.7 standard deviations in *y*, so within expected variation.

The distortion models are included in the KAI data-reduction pipeline, which is available for download to process Keck images.

Acknowledgments

We would like to thank the reviewer for their helpful comments. This work is part of the KAPA upgrade to the Keck I adaptive optics system. It was supported by funding from the National Science Foundation (NSF grant No. 1836016) and the Gordon and Betty Moore Foundation (grant No. GBMF 20200302-01).

The data presented herein were obtained at the W. M. Keck Observatory, which is operated as a scientific partnership among the California Institute of Technology, the University of California, and the National Aeronautics and Space Administration. The Observatory was made possible by the generous financial support of the W. M. Keck Foundation.

The authors wish to recognize and acknowledge the very significant cultural role and reverence that the summit of Maunakea has always had within the indigenous Hawaiian community. We are most fortunate to have the opportunity to conduct observations from this mountain.

Appendix Distortion Model Coefficients

The coefficients for the 5th-order Legendre polynomials for the 2020 and 2021 solutions are published in Tables 6 and 7. They are listed in the order of a `Legendre2D` object from the Python package `astropy.modeling.models`.









Table 6
2020 Distortion Model Coefficients

x Coefficient		y Coefficient	
c0_0	-12.579949944783726	c0_0	-0.813555426426706
c1_0	1.0237916547587298	c1_0	-0.0022164387375163083
c2_0	-1.5999180394334325e-05	c2_0	1.9357229722130354e-06
c3_0	6.285766160692843e-09	c3_0	-8.626958400313311e-10
c4_0	-1.8947060982249434e-12	c4_0	1.4779440923593954e-13
c5_0	2.019996218580465e-16	c5_0	-7.297539393357425e-18
c0_1	0.016365793581588697	c0_1	1.0019246497443028
c1_1	3.351989342060608e-05	c1_1	1.6916131971116817e-06
c2_1	-5.4667454189941535e-08	c2_1	-7.256053829527528e-10
c3_1	3.7137428663706565e-11	c3_1	6.882075809622699e-14
c4_1	-1.100479491906763e-14	c4_1	1.4757946020844489e-18
c5_1	1.1614681986800426e-18	c5_1	-1.000924875399054e-21
c0_2	5.513532196464921e-06	c0_2	-1.0941161744103507e-06
c1_2	-8.108842309839322e-08	c1_2	-3.5883060730058652e-09
c2_2	1.3204674091403965e-10	c2_2	9.167831954078092e-12
c3_2	-8.924787842347296e-14	c3_2	-9.900781522926062e-15
c4_2	2.5989963795498648e-17	c4_2	3.719523554955087e-18
c5_2	-2.6833391471909877e-21	c5_2	-4.336226149699189e-22
c0_3	-1.0338795766033258e-08	c0_3	1.0984969058443707e-09
c1_3	6.578873176698849e-11	c1_3	2.7355656297725758e-12
c2_3	-1.0934991961883518e-13	c2_3	-1.1820844178786653e-14
c3_3	7.409415616398766e-17	c3_3	1.2380655582233702e-17
c4_3	-2.1343236658327377e-20	c4_3	-4.367654393943676e-21
c5_3	2.1674921756875772e-24	c5_3	4.860491026860071e-25
c0_4	3.3091275704968904e-12	c0_4	-3.7929091402519257e-13
c1_4	-2.1424560329710686e-14	c1_4	-9.468596165191884e-16
c2_4	3.618574365270248e-17	c2_4	4.930078338930161e-18
c3_4	-2.4544010313123278e-20	c3_4	-4.866564089407131e-21
c4_4	7.019014066794706e-24	c4_4	1.6225916329453811e-24
c5_4	-7.052536509132523e-28	c5_4	-1.7274535537129371e-28
c0_5	-3.696672136580122e-16	c0_5	4.3881535626941096e-17
c1_5	2.423895817929673e-18	c1_5	1.143017060383648e-19
c2_5	-4.124442269088967e-21	c2_5	-6.410641705226948e-22
c3_5	2.7916995348645895e-24	c3_5	6.026389479859672e-25
c4_5	-7.934374097656221e-28	c4_5	-1.9188105928425224e-28
c5_5	7.912003914758666e-32	c5_5	1.9637967203417168e-32

Table 7
2021 Distortion Model Coefficients

x Coefficient		y Coefficient	
c0_0	-16.13650746183773	c0_0	0.822033544901506
c1_0	1.025742808777954	c1_0	-0.004308253857102781
c2_0	-1.5096220464060057e-05	c2_0	6.635813864989394e-06
c3_0	6.038824207496953e-09	c3_0	-4.615373022421915e-09
c4_0	-1.9275677088386118e-12	c4_0	1.3635691536552781e-12
c5_0	2.1439704436295304e-16	c5_0	-1.4447391742056619e-16
c0_1	0.021542262280615634	c0_1	0.9981122107526805
c1_1	2.5257225997377294e-06	c1_1	2.1541928177124362e-05
c2_1	3.1209687373207806e-09	c2_1	-3.809900837241432e-08
c3_1	-4.57661838226081e-12	c3_1	2.784296767763545e-11
c4_1	1.6086305134219583e-15	c4_1	-8.878807033551822e-15
c5_1	-1.8017735589880497e-19	c5_1	1.0052187823457118e-18
c0_2	-3.342955586436172e-06	c0_2	2.764344264932047e-06
c1_2	-6.512419349192539e-09	c1_2	-3.204584475163823e-08
c2_2	-7.318089229250518e-12	c2_2	5.824463646381393e-11
c3_2	9.622650181936157e-15	c3_2	-4.5541732039093786e-14
c4_2	-3.4272740753262777e-18	c4_2	1.516176525675083e-17
c5_2	4.089174614840367e-22	c5_2	-1.749043318162225e-21
c0_3	-2.8291754392429303e-09	c0_3	-1.3941684126774634e-09
c1_3	2.878787278998676e-12	c1_3	1.821406667180421e-11
c2_3	5.913637157270285e-15	c2_3	-3.566834122084455e-14
c3_3	-6.287054991922877e-18	c3_3	2.920334214220101e-17
c4_3	2.258882635823376e-21	c4_3	-9.839371221717718e-21
c5_3	-2.8848184195315455e-25	c5_3	1.1316912050886174e-24
c0_4	6.591323697471191e-13	c0_4	3.60036476517051e-13
c1_4	1.0754813225729936e-16	c1_4	-4.757578502398424e-15
c2_4	-2.441457020606532e-18	c2_4	9.970552932763727e-18
c3_4	1.984603287469064e-21	c3_4	-8.239987855583792e-21
c4_4	-6.801598882159653e-25	c4_4	2.7357561382872826e-24
c5_4	8.841040733625146e-29	c5_4	-3.0875684649468167e-28
c0_5	-4.770076372408685e-17	c0_5	-3.7639580340086116e-17
c1_5	-1.176876695689049e-19	c1_5	4.803496684844826e-19
c2_5	3.542634556372398e-22	c2_5	-1.0490794450794462e-21
c3_5	-2.454791660809844e-25	c3_5	8.519158816306318e-25
c4_5	7.945358162788551e-29	c4_5	-2.74434840326458e-28
c5_5	-1.0138129871855289e-32	c5_5	3.010910143124552e-32

ORCID iDs

Matthew S. R. Freeman  <https://orcid.org/0000-0001-6384-7450>
 Jessica R. Lu  <https://orcid.org/0000-0001-9611-0009>
 Abhimat Gautam  <https://orcid.org/0000-0002-2836-117X>
 Renate Kupke  <https://orcid.org/0000-0002-5826-5314>
 Andrea Ghez  <https://orcid.org/0000-0003-3230-5055>
 Shoko Sakai  <https://orcid.org/0000-0001-5972-663X>
 Jay Anderson  <https://orcid.org/0000-0003-2861-3995>
 Andrea Bellini  <https://orcid.org/0000-0003-3858-637X>

References

- Anderson, J., & King, I. R. 2002, *PASP*, 115, 113
 Anderson, J., Sarajedini, A., Bedin, L. R., et al. 2008, *AJ*, 135, 2055
 Bellini, A., Anderson, J., van der Marel, R. P., et al. 2014, *ApJ*, 797, 115
 Diolaiti, E., Bendinelli, O., Bonaccini, D., et al. 2000, *Proc. SPIE*, 4007, 879
 Ghez, A. M., Salim, S., Weinberg, N. N., et al. 2008, *ApJ*, 689, 1044
 Groth, E. J. 1986, *AJ*, 91, 1244
 Jia, S., Lu, J. R., Sakai, S., et al. 2019, *ApJ*, 873, 9
 Lam, C. Y., Lu, J. R., Udalski, A., et al. 2022, *ApJL*, 933, L23
 Larkin, J., Barczys, M., Krabbe, A., et al. 2006, *Proc. SPIE*, 6269, 62691A
 Lu, J. 2022, Keck-DataReductionPipelines/KAI: v1.0.0 Release of KAI, v1.0.0, Zenodo, doi:10.5281/zenodo.6522913
 Lu, J. R., Sinukoff, E., Ofek, E. O., Udalski, A., & Kozłowski, S. 2016, *ApJ*, 830, 41
 Plewa, P. M., Gillessen, S., Bauböck, M., et al. 2018, *RNAAS*, 2, 35
 Rampy, R., Femenia, B., Lyke, J., et al. 2015, in *Adaptive Optics for Extremely Large Telescopes 4—Conf. Proc.* (Los Angeles, CA: UCLA),
 Service, M., Lu, J. R., Campbell, R., et al. 2016, *PASP*, 128, 095004
 Service, M., Lu, J. R., Chun, M., et al. 2019, *JATIS*, 5, 039005
 Stolte, A., Ghez, A. M., Morris, M., et al. 2008, *ApJ*, 675, 1278
 Terry, S. K., Lu, J. R., Turri, P., et al. 2023, *JATIS*, 9, 018003
 van Leeuwen, F., de Bruijne, J. H. J., Arenou, F., et al. 2018, Gaia DR2, <https://gea.esac.esa.int/archive/documentation/GDR2/>
 Witzel, G., Lu, J. R., Ghez, A. M., et al. 2016, *Proc. SPIE*, 9909, 990910
 Wizinowich, P., Chin, J., Correia, C., et al. 2020, *Proc. SPIE*, 11448, 114480E
 Wizinowich, P., Smith, R., Biasi, R., et al. 2014, *Proc. SPIE*, 9148, 91482B
 Yelda, S., Lu, J. R., Ghez, A. M., et al. 2010, *ApJ*, 725, 331